

CANGAROO-III Observations of the 2006 Outburst of PKS 2155–304

Y. Sakamoto¹, K. Nishijima², T. Mizukami³, E. Yamazaki², J. Kushida², R. Enomoto⁴,
M. Ohishi⁴, G.V. Bicknell⁵, R.W. Clay⁶, P.G. Edwards⁷, S. Gunji⁸, S. Hara⁹, T. Hattori²,
S. Hayashi¹⁰, Y. Higashi³, Y. Hirai¹¹, K. Inoue⁸, C. Itoh¹², S. Kabuki³, F. Kajino¹⁰,
H. Katagiri¹³, A. Kawachi², T. Kifune⁴, R. Kiuchi⁴, H. Kubo³, R. Mizuniwa², M. Mori⁴,
H. Muraishi¹⁴, T. Naito¹⁵, T. Nakamori³, S. Nakano³, D. Nishida³, A. Seki²,
V. Stamatescu⁶, T. Suzuki¹¹, D.L. Swaby⁶, T. Tanimori³, G. Thornton⁶, F. Tokanai⁸,
K. Tsuchiya³, S. Watanabe³, Y. Yamada¹⁰, S. Yanagita¹¹, T. Yoshida¹¹, T. Yoshikoshi⁴,
and Y. Yukawa⁴

kyoshi@tkikam.sp.u-tokai.ac.jp

ABSTRACT

We have used the CANGAROO-III imaging atmospheric Cherenkov telescopes to observe the high-frequency-peaked BL Lacertae (HBL) object

¹Graduate School of Science and Technology, Tokai University, Hiratsuka, Kanagawa 259-1292, Japan

²Department of Physics, Tokai University, Hiratsuka, Kanagawa 259-1292, Japan

³Department of Physics, Graduate School of Science, Kyoto University, Sakyo-ku, Kyoto 606-8502, Japan

⁴Institute for Cosmic Ray Research, University of Tokyo, Kashiwa, Chiba 277-8582, Japan

⁵Research School of Astronomy and Astrophysics, Australian National University, ACT 2611, Australia

⁶Department of Physics and Mathematical Physics, University of Adelaide, SA 5005, Australia

⁷Paul Wild Observatory, CSIRO Australia Telescope National Facility, Locked Bag 194, Narrabri, NSW 2390, Australia

⁸Department of Physics, Yamagata University, Yamagata, Yamagata 990-8560, Japan

⁹Ibaraki Prefectural University of Health Sciences, Ami, Ibaraki 300-0394, Japan

¹⁰Department of Physics, Konan University, Kobe, Hyogo 658-8501, Japan

¹¹Faculty of Science, Ibaraki University, Mito, Ibaraki 310-8512, Japan

¹²National Institute of Radiological Sciences, Chiba, Chiba 263-8555, Japan

¹³Department of Physical Science, Graduate School of Science, Hiroshima University, Higashi-Hiroshima, Hiroshima 739-8526, Japan

¹⁴School of Allied Health Sciences, Kitasato University, Sagamihara, Kanagawa 228-8555, Japan

¹⁵Faculty of Management Information, Yamanashi Gakuin University, Kofu, Yamanashi 400-8575, Japan

PKS 2155–304 between 2006 July 28 (MJD 53944) and August 2, triggered by the H.E.S.S. report that the source was in a high state of TeV gamma-ray emission. A signal was detected at the 4.8σ level in an effective live time of 25.1 hours during the outburst period. The flux of Very High Energy gamma-rays from the CANGAROO-III observations shows the variability on the time scale of less than a few hours. The averaged integral flux above 660 GeV is $(1.6 \pm 0.3_{stat} \pm 0.5_{syst}) \times 10^{-11} \text{ cm}^{-2} \text{ sec}^{-1}$ which corresponds to $\sim 45\%$ of the flux observed from the Crab nebula. Follow-up observations between August 17 (MJD 53964) and 25 indicate the source activity had decreased.

Subject headings: Galaxies: active — BL Lacertae objects: Individual: PKS 2155–304 — Gamma rays: observations

1. Introduction

The most astonishing contribution from the ground-based IACTs has been the detection of AGNs at energies above several hundred GeV. To date, 19 active galactic nuclei have been reported to emit Very High Energy (VHE) gamma-rays (Hinton 2007), most of them classified as high-frequency-peaked BL Lacs (HBLs) (Padovani & Giommi 1995). Some, such as Mrk 421 and Mrk 501, have been targets of simultaneous multi-wavelength campaigns since their first TeV detection (Punch et al. 1992; Quinn et al. 1996), and are well studied. The derived broadband spectral energy distributions (SEDs) show that they have two components. The lower energy component is believed to be synchrotron emission produced by relativistic electrons in the jet, and the higher energy component, although relatively poorly understood, is probably explained by the inverse-Compton scattering of seed photons (either synchrotron or ambient photons) by the same population of electrons (see e.g., Jones, O’deh & Stein 1974; Ulrich, Maraschi, & Urry 1997; Dermer & Schlickeiser 1993; Sikora, Begelman & Rees 1994).

Multi-wavelength observations of HBLs have also shown that the fluxes are extremely variable, particularly in the higher energy bands. Flux variations on a wide range of time scales from months to two minutes are reported at TeV energies (e.g., Gaidos et al. 1996; Krawczynski et al. 2001; Aharonian et al. 2002, 2005c; Blazejowski et al. 2005; Aharonian et al. 1999; Gliozzi et al. 2006; Albert et al. 2007a). Time variability is a very useful way to probe the emission mechanism in the jet. Characteristic time scales, which can be employed as a measure of super-massive black hole mass at the center of HBL, have been studied with X-ray data using statistical techniques such as power spectra, structure functions, *etc* (e.g., Hayashida et al. 1998; Zhang et al. 1999; Kataoka et al. 2001; Cui 2004). A good corre-

lation of the X-ray and the TeV fluxes has also been reported (e.g., Buckley et al. 1996; Takahashi et al. 1996; Djannati-Atai et al. 1999; Takahashi et al. 2000; Sambruna et al. 2000; Krawczynski et al. 2002; Albert et al. 2007a). Recently, however, poor correlations or a total lack of correlation between the X-ray and TeV fluxes of individual flares have been observed (e.g., Blazejowski et al. 2005; Aharonian et al. 2005c), and even TeV flares with no X-ray counterpart have been found (Blazejowski et al. 2005; Krawczynski et al. 2004). Spectral hardening with flux in the TeV energy range has been reported for Mrk 421 (Aharonian et al. 2002; Krennrich et al. 2002; Albert et al. 2007a) and Mrk 501 (Albert et al. 2007b).

PKS 2155–304 ($z = 0.116$ (Falomo et al. 1993)) is one of the brightest BL Lacs in the X-ray (Brinkmann et al. 1994; Kubo et al. 1998; Giommi et al. 1998; Vestrand & Sreekumar 1999; Nicastro 2002; Zhang et al. 2005) and EUV (Marshall, Carone, & Fruscione 1993) bands. Since the discovery of X-ray emission from this object (Griffiths et al. 1979; Schwartz et al. 1979), it has been repeatedly observed over a wide range of frequencies from radio to Very High Energy (VHE) gamma-rays (e.g., Treves et al. 1989; Vestrand, Stacy, & Sreekumar 1995; Zhang & Xie 1996; Pian et al. 1997; Piner & Edwards 2004; Dominici et al. 2004; Aharonian et al. 2005a).

In 1997 November, a gamma-ray and X-ray outburst from PKS 2155–304 was detected by EGRET (Sreekumar & Vestrand 1997), BeppoSAX (Chiappetti et al. 1999) and RXTE (Vestrand & Sreekumar 1999). During this active phase, the Durham group observed PKS 2155–304 using their Mark 6 telescope, and reported the first detection of VHE gamma-rays at the 6.8σ level above 300 GeV (Chadwick et al. 1999a) at the time of BeppoSAX observation. However they found no evidence for TeV gamma-ray emission during observations in 1998 (Chadwick et al. 1999b) when the X-ray flux level was low. PKS 2155–304 was observed with the CANGAROO-I 3.8 m telescope in 1997, though poor weather resulted in minimal overlap with the Durham observations. No gamma-ray signal above 1.5 TeV was detected (Roberts et al. 1999). PKS 2155–304 was further observed in 1999, 2000 and 2001 with the CANGAROO-II telescope. It remained in a low state of X-ray activity in those periods, and was not detected above the energy threshold of 420 GeV (Nishijima et al. 2001; Nishijima 2002; Nakase et al. 2003). PKS 2155–304 was confirmed as a TeV gamma-ray source by the H.E.S.S. group in 2004. They reported a 45σ detection at energies greater than 160 GeV in July and October, 2002, and June–September, 2003 (Aharonian et al. 2005a). The flux variability on time scales of months, days, and hours were also reported, and the monthly-averaged flux above 300 GeV was between 10% and 60% of Crab flux. The energy spectrum was characterized by a steep power law with a time-averaged photon index of $\Gamma \sim 3.3$. Multi-wavelength observations in 2003 in a low state showed no correlation between the X-ray and the gamma-ray fluxes, or between any other wavebands, even though the fastest ever X-ray flare in this object, with a 1500 sec timescale, was detected (Aharonian et al. 2005b).

In July 2006, the H.E.S.S. group reported that PKS 2155–304 had been detected at historically high TeV flux levels of up to several crab (Benbow et al. 2006; Raue et al. 2006). They also presented very rapid flux variability with one-minute time scale resolution and found well-resolved bursts varying on timescales of ~ 200 seconds (Aharonian et al. 2007). The H.E.S.S. report triggered multi-wavelength Target of Opportunity (ToO) observations, including the observations with the CANGAROO-III telescopes from 2006 July 28 (MJD 53944) described in this paper.

Numerous multi-wavelength campaigns of PKS 2155–304 have been carried out (e.g., Edelson et al. 1995; Urry et al. 1997; Aharonian et al. 2005b), and many physical implications for the emission mechanisms have been reported (e.g., Chiappetti et al. 1999; Kataoka et al. 2000; Edelson et al. 2001; Tanihata et al. 2001; Zhang et al. 2002, 2006). However, these models are still face challenges in explaining the complex and different patterns of multi-wavelength variations for each epoch.

For objects like PKS 2155–304 which show rapid and complex time variability, continuous monitoring is very important for modeling the emission mechanisms. The difference in longitude between the H.E.S.S. and CANGAROO-III sites is $\sim 120^\circ$, corresponding to an 8 hour time difference. Thus the H.E.S.S. and the CANGAROO-III data complement one another. Northern hemisphere blazars, such as Mrk 421, Mrk 501 and 1ES 1959+650, have been observed at TeV energies continuously with more than two geographically distant telescope systems (e.g., Rebillot et al. 2006; Gliozzi et al. 2006; Krawczynski et al. 2004), providing greatly improved time coverage, but PKS 2155–304 is the first object in the southern sky for which such studies have been made.

2. Detector and Observations

The CANGAROO-III imaging atmospheric Cherenkov telescope system which consists of four telescopes are operated in Woomera, South Australia (longitude $136^\circ 47' \text{E}$, latitude $31^\circ 06' \text{S}$, 160 m a.s.l.). They have parabolic reflectors of 10 m diameter with an 8 m focal length. Each reflector consists of 114 small spherical mirrors of 80 cm diameter, which are made of Fiber Reinforced Plastic. The imaging cameras have 427 pixels of 0.17° size and a total field of view of $\sim 4^\circ$. These telescopes use altitude-azimuth mounts and are placed at the corners of a diamond with 100 m sides. The details of the mirror, the camera, and the total performance of the light collecting system are described in Kawachi et al. (2001), Kabuki et al. (2003), and Enomoto et al. (2006a).

The CANGAROO-III observations of PKS 2155–304 during this outburst period were

made on five moonless nights between July 28 (MJD 53944) to August 2 in 2006. There were no observations on August 1, and the July 29 observations were affected by cloud. Three (T2, T3, T4) of the four telescopes were used in these observations. For each telescope, when the number of hit pixels exceeds four within a 20 nsec coincidence window, a local trigger is sent to the stereo trigger system through an optical link. In the stereo trigger system, determination of stereo events is done by requiring that at least two local trigger signals coinciding for at least 10 nsec within a 650 nsec time window, taking the geometrical time delay, which depends on the telescope pointing direction, into consideration (Kubo et al. 2001; Nishijima et al. 2005).

These observations were made using wobble mode in which pointing position of each telescope was shifted in declination between $\pm 0.5^\circ$ from the center of PKS 2155–304 alternatively every twenty minutes. Due to a mechanical tracking problem with the T3 telescope during this period, stereo observations with three telescopes were done only after culmination. Stereoscopic observations using T2 and T4, which are located on the long diagonal of the diamond, were performed before culmination from July 28 to July 31.

The details of the CANGAROO-III observations of PKS 2155-304 are summarized in Table 1. The typical trigger rates, the mean zenith angle, and the total observation time of two-fold coincidences of T2–T4 were ~ 20 Hz, 26.6° , and 11.4 hours, respectively. The typical trigger rate of three-fold coincidences was ~ 12 Hz, with a mean zenith angle for these observations of 20.4° and a total observation time of 17.6 hours. The daily observation time t_{obs} , average zenith angle z , and trigger rate r_{tr} are shown in Table 1 for both T2–T4 and three-fold data. The zenith angles of observations ranged from 52° to 7° for T2–T4 data, and from 1° to 46° for three-fold data.

Follow-up observations were made with the same system on six moonless nights between August 17 (MJD 53964) and 25. These data were taken only after culmination using three-fold coincidences. The zenith angle during these observations ranged from 1° to 48° with a mean of 20.9° , and a total observation time of 19.1 hours. These observations are also summarized in Table 1.

3. Analysis

In order to calibrate the relative gain and the timing for each pixel, the data taken by illuminating the focal plane uniformly with LED photons were used. Conversion factors from ADC value to photoelectrons for each pixel are determined using the LED system in the camera vessel, and the timing jitter of the pulse signals are calibrated using light from a

LED mounted at the center of the telescope dish. Details of the standard CANGAROO-III calibration methods are given in Kabuki et al. (2003). These LED runs were performed at least once per night. Five out of 427 pixels for T2 and two for T3 were identified as bad pixels which gave no signal or false signals, and these were removed from the analysis. There were no bad pixels in the T4 camera.

We have cleaned the images to eliminate night sky background photons and select shower images. Each pixel is required to have a signal larger than 5.0 p.e. with an arrival time within ± 30 nsec of the average shower arrival time. Images containing at least five adjacent pixels which pass the above requirements are selected. The distributions of shower rate each minute are shown in Fig. 1 for T2–T4 coincidence (left panel) and three-fold coincidence (right panel), respectively, and the average shower rate r_{sh} for each night is listed in Table 2. In order to ensure reliable arrival direction and energy estimations, the data taken during periods when shower rate was lower than ~ 5 Hz for three-fold coincidences and ~ 10 Hz for T2–T4 coincidences are not used, as they are probably affected by clouds. In the following analysis, we further require that none of the brightest 15 pixels of each image should be in the outermost layer of the camera in order to avoid deformation of the image. This method improves the effective area by more than 20% compared to the previous simple edge cut (Enomoto et al. 2006a), particularly above ~ 2 TeV. After taking into account the DAQ dead-time, the effective total live time t_{liv} is also summarized in the same table.

The moments of the shower image are then parameterized using the *Hillas parameters* (Hillas et al. 1985), and the arrival directions are reconstructed using the intersection of image axes. The intersection point is obtained by minimizing the sum of squared widths of the images seen from the assumed point with a constraint on the distances between images' center of gravity and assumed intersection point (IP-fit) considering the *length/width* ratio (see Kabuki et al. (2007) for details), which is similar to Algorithm 5 in Hofmann et al. (1999). This method improves the signal to noise ratio by more than 10% compared to the procedure described in Enomoto et al. (2006a) and is confirmed by Monte Carlo simulations and observations of the Crab nebula.

After event reconstruction, numerous cosmic ray background events are rejected using the Fisher Discriminant (FD) method (Fisher 1936). The FD value for each event is calculated as explained in Enomoto et al. (2006b) using the size-corrected *width* and *length* for each telescope, where the energy dependence of the *width* and *length* are corrected to keep each parameter at the same values in various energies. In order to determine the optimum FD cut values, a Monte Carlo simulation was carried out assuming a single power-law spectrum, $dF/dE \propto E^{-\Gamma}$, with an index of $\Gamma = 3.3$, as determined for PKS 2155–304 by the H.E.S.S. group (Aharonian et al. 2005a). Before applying the FD cuts, the data are

divided into two data sets, "2fold" which include the data taken by only T2–T4 coincidence and "3fold" which required a three-fold coincidence between the three telescopes. Each dataset is further divided by zenith angle into two datasets, "3fold–SZ" and "2fold–SZ" for $z < 30^\circ$, and "3fold–LZ" and "2fold–LZ" for $z > 30^\circ$, respectively. Considering the Point Spread Function (PSF) of 0.23° (FWHM), the θ^2 (where θ is the angular difference between the reconstructed arrival direction and the source position) cuts were applied at $\theta^2 < 0.06 \text{ deg}^2$ for the 3fold data, and to keep the same efficiency for gamma rays as for the three-fold analysis, $\theta^2 < 0.14 \text{ deg}^2$ was applied to the 2fold data. Based on the Monte Carlo simulation assuming 100 % Crab flux of gamma rays above 600 GeV, we could determine the best FD cut criteria which yielded the highest significance for each dataset. Following the results from the Monte Carlo study, we select the events with $FD > -0.3$ for 3fold–SZ, $FD > -0.2$ for 3fold–LZ, $FD > -0.1$ for 2fold–SZ and $FD > -0.2$ for 2fold–LZ datasets, as candidate gamma-ray events.

The primary gamma-ray energy is estimated from the number of detected photo-electrons, based on the Monte Carlo simulations assuming a single power-law spectrum as mentioned above. This relation depends on the zenith angle of observations, so the simulations were done using the same variation of elevation as the actual observations. Although there is also some dependence on the impact parameter in the energy determination, we do not incorporate that here, with the resulting energy resolution estimated to be 30 % around 1 TeV. The effective detection area has been estimated from the Monte Carlo simulation as a function of energy. The detection energy threshold E_{th} is taken to be the energy of the peak of the distribution of triggered shower energies.

4. Results

In this section, we show the results of CANGAROO-III observations of PKS 2155–304 in 2006. A summary of the results are shown in Table 2. Using these results, we present the average integral flux, the average differential energy spectrum, and the time variation.

4.1. Average flux

After the data reduction described in previous section, the final θ^2 distribution is obtained. Fig. 2 (a) and (c) show the results in the outburst period for 3fold and 2fold datasets, respectively. The background level was estimated using off-source data in the corresponding region in the other side of the field of view. The distributions of the excess events

against θ^2 , i.e., with the off-source events subtracted from the on-source events, are shown in Fig. 2(b) and (d) for *3fold* and *2fold*, respectively. There are clear excesses at small values of θ^2 in both figures corresponding to the observed signal from PKS 2155–304. The number of excess events are calculated using a circular region of $\theta^2 < 0.06 \text{ deg}^2$ for *3fold* and $\theta^2 < 0.14 \text{ deg}^2$ for *2fold* centered on the source position, respectively, considering the PSF as mentioned in the previous section. The hatched histograms in figure 2 (b) and (d) indicate the expected PSF normalized to the number of excess events in $\theta^2 < 0.25$. The combined excess of all the data is 322 ± 67 events (4.8σ), where only the propagation of statistical errors is considered. Fig. 3 shows the FD distributions after the θ^2 cut for on-source events, off-source events and the gamma-ray candidate events (on-source–off-source) together with the Monte-Carlo gamma-rays normalized to the number of excess events. The FD distributions are quite consistent for the observed gamma-ray events and the Monte Carlo gamma rays. The FD cut is not applied for this plot. The time-averaged integral flux above 660 GeV is calculated to be $F(> 660 \text{ GeV}) = (1.6 \pm 0.3_{stat} \pm 0.5_{syst}) \times 10^{-11} \text{ cm}^{-2} \text{ sec}^{-1}$. This corresponds to $\sim 45\%$ of the flux observed from the Crab nebula (Aharonian et al. 2004), and is a factor of five more intense than the flux in the low state reported in (Aharonian et al. 2005a). The systematic error in the flux arises mainly from energy scale uncertainties due to the absolute light collection efficiency (20%), FD cut criteria (22%), uncertainties in the probability density function of images generated by Monte Carlo simulation (10%), and the uncertainty of a power law index (8%). At a higher energy threshold above 1.0 TeV, which corresponds to the energy threshold for *3fold-LZ* and *2fold-LZ* data, no significant excess above our sensitivity from PKS 2155–304 is found in this period, and the resulting 2σ flux upper limit is $F(> 1.0 \text{ TeV}) < 9.2 \times 10^{-12} \text{ cm}^{-2} \text{ sec}^{-1}$.

For a cross-check, an alternative analysis using the Fisher Discriminant with a fit (Enomoto et al. 2006b) was performed on the same data. Although this is our standard method of analysis, the fine time binning and consequent small count statistics make it difficult to estimate the systematic errors correctly. The main source of error is the non-uniformity of the Fisher Discriminant in the ring-shaped background region. So we primarily took a conservative FD cuts method using a single reflected background at the expense of the statistics, and used FD fits as a cross-check. The difference of the integral flux between them was less than 15% comparing at the same threshold energy.

4.2. Average differential energy spectrum

We obtained the time-averaged differential energy spectrum from all the data except for large zenith angle dataset, *i.e.* from *3fold-SZ* and *2fold-SZ*, since the large zenith angle

data have a higher energy threshold and therefore lower energy bins have a different exposure than higher energy one. The differential flux is shown in Fig. 4 as closed circles with 1σ statistical error bars. The best fit of a power law to the small zenith angle data yields a photon index $\Gamma = 2.5 \pm 0.5_{stat} \pm 0.7_{syst}$ and a flux normalization $N_0(1 \text{ TeV}) = (1.0 \pm 0.2_{stat} \pm 0.3_{syst}) \times 10^{-11} \text{ cm}^{-2} \text{ sec}^{-1} \text{ TeV}^{-1}$. We estimate the systematic error considering the same factors as mentioned in the previous section.

4.3. Time variations

We have searched for gamma-ray emission from PKS 2155–304 on a night-by-night basis. The live time, t_{liv} , the number of on-source and off-source events, N_{ON} and N_{OFF} , the number of excess events, N , and significance, s , corresponding to each night are summarized in Table 2. Here the off-source data are summed up over the five nights to reduce the statistical fluctuation, and normalized to the live time of each night. The nightly average integral fluxes F above 660 GeV, using all the data are also shown in the same table, and are plotted in Fig. 5, where the flux from *3fold* and *2fold* datasets are combined. The light curve shows that the average flux reached $\sim 70\%$ Crab in the night of July 30. Assuming a constant average flux, a χ^2 fit yields a value of 13.9 for 4 degrees of freedom, which corresponds to a χ^2 probability of $\sim 0.8\%$. This means that there is a marginal time variations of the average flux on a nightly basis between July 28 and August 2.

We further divide the data into ~ 40 minutes bins for each night, and intra-night variation is investigated. Since the pointing offset from the source position is alternated in sign every 20 minutes in our observations, 40 minutes bin is adopted as it offers a reasonable cancellation of any asymmetric effects. The light curve of PKS 2155–304 expressed by the integral flux of VHE gamma-rays above 660 GeV using *2fold-SZ* and *3fold-SZ* dataset is shown in Fig. 6.

Assuming a constant average flux for the data above 660 GeV, a χ^2 fit yields a value of 96.4 for 30 degrees of freedom, which corresponds to a χ^2 probability of 7×10^{-9} . The same calculation was done for the data of July 28 and 30, and gave χ^2 values of 29.2 and 22.1 for 6 degrees of freedom, respectively. The intra-night variations are apparent. From figure 6, although it is difficult to calculate the fractional root mean square variability amplitude F_{var} (Vaughan et al. 2003) because of the poor statistics, $F_{var} = 0.75 \pm 0.07$ on July 28 and 0.58 ± 0.08 on July 30 are obtained.

The results in the follow-up observations between August 17 and 25 are also summarized in Table 2. The 2σ upper limit above 680 GeV is $F(> 680 \text{ GeV}) < 6.8 \times 10^{-12} \text{ cm}^{-2} \text{ sec}^{-1} (<$

20% Crab), which shows TeV gamma-ray activity had subsided compared to the outburst period.

5. Discussion

From Figure 5, the fluxes on July 28 and 30 exceed 50% of the flux from the Crab nebula, and are the same level as that at the end of July 27–28 (MJD 53944) observation reported by the H.E.S.S. group (Aharonian et al. 2007), taking into account the difference of energy threshold and assuming a power law spectrum. The flux in July 29 might be underestimated due to the presence of clouds. Therefore, our light curve suggests that the flux continuously decreases on average following the large flare of July 28. The preliminary H.E.S.S. light curve above 200 GeV presented by Raue et al. (2006) indicates that a 5 crab flare occurred between our observations of July 29 and 30. However we did not detect a flare in this period, possibly due to the 10 hour gap between the end of the H.E.S.S. observations and the start of our observations. For the shorter variability time scales, the July 28 and 30 data indicate the intra-night variations.

The derived values of the fractional root mean square variability amplitude, $F_{var} = 0.49$ for night by night variation and $F_{var} = 0.47$ for intra-night variation in July 28, are comparable to the values from the intra-night variability earlier on July 28 reported by H.E.S.S. (Aharonian et al. 2007). They are rather higher than the values for the X-ray variability (e.g., 0.10–0.43 listed by Zhang et al. (1999)), (although much higher, and energy dependent, values of F_{var} have been reported by MAGIC (Albert et al. 2007b) for Mrk 501).

In Figure 7, our TeV light curve is plotted together with the *Swift* x-ray light curve (Foschini et al. 2007). Unfortunately, *Swift* started observations two hours after CANGAROO stopped observing each day, so there are no simultaneous observations. There is no evident correlation between the X-ray and the gamma-ray fluxes, with a time lag of approximately 9 hours. Foschini et al. (2007) reported the X-ray flux increased by a factor of 5 in the 0.3–10 keV energy band without a large spectral change, and the highest peak of the *Swift* light curve corresponds to the second large TeV flare observed by H.E.S.S. (Raue et al. 2006). The X-ray flux in this outburst is not very high and it is not possible to detect time variation of the flux in the RXTE–ASM data. For observations in 2002 and 2003, no correlation between the X-ray and the gamma-ray fluxes was reported by H.E.S.S. (Aharonian et al. 2005b), however a strong correlation during 2004 observations was presented in a preliminary analysis by Punch et al. (2007). On the other hand, Mrk 421 has displayed a good correlation between the X-ray and the gamma-ray fluxes, although recently no correlation results, including “Orphan flares”, were reported. The simple one-zone SSC model is unable

to explain such complex behavior (e.g., Blazejowski et al. 2005). Some models explaining “Orphan flares” have been proposed, for example, by Kusunose & Takahara (2006) for the leptonic model and Böttcher (2005) for the hadronic model.

During the outburst periods, the photon index may change along with the flux variations, as is the case for Mrk 421 and Mrk 501 (e.g., Aharonian et al. 2002; Krennrich et al. 2002; Albert et al. 2007a,b). However, the average photon index we obtained here does not differ from the value that H.E.S.S. reported previously (Aharonian et al. 2005a) within errors, and is consistent with those subsequently reported by H.E.S.S. (Aharonian et al. 2007) and MAGIC (Mazin & Lindfors 2007). The reason for this difference in the variation of photon index between PKS 2155–304 and Mrk 421 is still an open question. Although the error on the spectrum is enormous, a spectral index after correction for the absorption by the extra-galactic background light is calculated to be $\Gamma = 1.6 \pm 0.5$ and $\Gamma = 1.3 \pm 0.5$ using the baseline model and the fast evolution model by Stecker & Scully (2006), respectively.

6. Conclusion

We observed the southern HBL PKS 2155–304 from 2006 July 28 (MJD 53944) to August 2 with the CANGAROO-III imaging Cherenkov telescopes. During the VHE high state we detected a signal at 4.8σ significance above 660 GeV in the total effective exposure time of 25.1 hours. The time averaged integral flux above 660 GeV is $(1.6 \pm 0.3_{stat} \pm 0.5_{syst}) \times 10^{-11} \text{ cm}^{-2} \text{ sec}^{-1}$ which corresponds to $\sim 45\%$ of the flux observed from the Crab nebula. The intra-night time variations of the flux were seen in our observations. Follow-up observations two weeks later indicated the source activity had decreased to lower than $\sim 20\%$ Crab flux..

We thank Dr. W. Hofmann, Dr. S. Wagner, Dr. G. Rowell, Dr. W. Benbow, Dr. B. Giebels, and L. Foschini for providing details of the H.E.S.S. and the Swift observations of PKS 2155–304. This work is supported by a Grant-in-Aid for Scientific Research by the Japan Ministry for Education, Culture, Sports, Science and Technology, the Australian Research Council (Grants LE0238884 and DP0345983), and Inter-University Research Program by the Institute for Cosmic Ray Research. The support of JSPS Research Fellowship for T.N. and Y.H. is gratefully acknowledged. A part of this work was funded for Y.S. by the Sasagawa Scientific Research Grant from The Japan Science Society.

REFERENCES

- Aharonian, F., et al. 1999, *A&A*, 342, 69
- Aharonian, F., et al. 2002, *A&A*, 393, 89
- Aharonian, F., et al. 2004, *ApJ*, 614, 897
- Aharonian, F., et al. 2005a, *A&A*, 430, 865
- Aharonian, F., et al. 2005b, *A&A*, 442, 895
- Aharonian, F., et al. 2005c, *A&A*, 437, 95
- Aharonian, F., et al. 2007, *ApJ*, 664, L71
- Albert, J., et al. 2007, *ApJ*, 663, 125
- Albert, J., et al. 2007, *ApJ*, submitted (astro-ph/0702008)
- Beilicke, M. 2006, presentation at the 3rd Workshop on the Nature of Unidentified High-Energy Sources (Barcelona)
- Benbow, W., Costamante, L., & Giebels, B. 2006, *ATel* #867
- Blazejowski, M., et al. 2005, *ApJ*, 630, 130
- Böttcher, M. 2005, *ApJ*, 621, 176
- Brinkmann, W., et al. 1994, *A&A*, 288, 443
- Buckley, J. H., et al. 1996, *ApJ*, 472, L9
- Chadwick, P. M., et al. 1999a, *ApJ*, 513, 161
- Chadwick, P. M., et al. 1999b, in *Proc. 26th Int. Cosmic Ray Conf. (Salt Lake City)*, 3, 338
- Chiappetti, L., et al. 1999, *ApJ*, 521, 552
- Cui, W. 2004, *ApJ*, 605, 662
- Dermer, C. D., & Schlickeiser, R. 1993, *ApJ*, 416, 458
- Djannati-Atai, A., et al. 1999, *A&A*, 350, 17
- Dominici, T. P., et al. 2004, *AJ*, 128, 47

- Edelson, R. A., et al. 1995, *ApJ*, 438, 120
- Edelson, R. A., et al. 2001, *ApJ*, 554, 274
- Enomoto, R., et al. 2006a, *ApJ*, 638, 397
- Enomoto, R., et al. 2006b, *ApJ*, 652, 1268
- Falomo, R. et al. 1993, *ApJ*, 411, L63
- Fisher, R. A. 1936, *Annals of Eugenics*, 7, 179
- Foschini, L., et al. 2007, *ApJ*, in press(astro-ph/0701868)
- Gaidos, J. A., et al. 1996, *Nature*, 383, 319
- Giebels, B. 2006, presentation at 2nd Workshop on TeV Particle Astrophysics (Madison)
- Giommi, P., et al. 1998, *A&A*, 333, L5
- Glozzi, M., et al. 2006, *ApJ*, 646, 61
- Griffiths, R. E., et al. 1979, *ApJ*, 234, 810
- Hayashida, K., et al. 1998, *ApJ*, 500, 642
- Hillas, A. M., et al. 1985 in *Proc. 19th Int. Cosmic Ray Conf. (La Jolla)*, 3, 445
- Hinton, J. 2007, in *Proc. of the 30th Int. Cosmic Ray Conf. (Merida)*, Rapporteur Talk
- Hofmann, W. et al. 1999, *Astropart. Phys.*, 122, 135
- Jones, T. W., O'dell, S. L., & Stein, W. A. 1974, *ApJ*, 188, 353
- Kabuki, S., et al. 2003, *NIM*, A500, 318
- Kabuki, S., et al. 2007, *ApJ*, 668, 968
- Kataoka, J., et al. 2000, *ApJ*, 528, 243
- Kataoka, J., et al. 2001, *ApJ*, 560, 659
- Kawachi, A., et al. 2001, *Astropart. Phys.*, 14, 261
- Krawczynski, H., et al. 2001, *ApJ*, 559, 187
- Krawczynski, H., et al. 2002, *MNRAS*, 336, 721

- Krawczynski, H., et al. 2004, *ApJ*, 601, 151
- Krennrich, F., et al. 2002, *ApJ*, 575, L9
- Kubo, H., et al. 1998, *ApJ*, 504, 693
- Kubo, H., et al. 2001, in Proc. 27th Int. Cosmic Ray Conf. (Hamburg), 2900
- Kusunose, M., & Takahara, F. 2006, *ApJ*, 651, 113
- Marshall, H. L., Carone, T. E., & Fruscione, A. 1993, *ApJ*, 414, L53
- Mazin, D., & Lindfors, E. 2007, in Proc. of the 30th Int. Cosmic Ray Conf. (Merida), OG2.3, #936
- Nakase, T. 2003, in Proc. 28th Int. Cosmic Ray Conf. (Tsukuba), 2587
- Nicastro, F. 2002, *ApJ*, 573, 157
- Nishijima, K. 2002, *PASA*, 19, 26
- Nishijima, K., et al. 2001, in Proc. 27th Int. Cosmic Ray Conf. (Hamburg), 2626
- Nishijima, K., et al. 2005, in Proc. 29th Int. Cosmic Ray Conf. (Pune), 15, 327
- Padovani, P., & Giommi, P. 1995, *ApJ*, 444, 567
- Pian, E., et al. 1997, *ApJ*, 486, 784
- Piner, E., & Edwards, P. G. 2004, *ApJ*, 600, 115
- Punch, M., et al. 1992, *Nature*, 358, 477
- Punch, M., et al. 2007, presented at the 27th Int. Cosmic Ray Conf. (Merida)
- Quinn, J., et al. 1996, *ApJ*, 456, L83
- Raue, M., et al. 2006, presented at the INTEGRAL Workshop on the keV to TeV Connection(Rome)
- Rebillot, P. F., et al. 2006, *ApJ*, 641, 740
- Roberts, M. D., et al. 1999, *A&A*, 343, 691
- Sambruna, R. M., et al. 2000, *ApJ*, 538, 127
- Schwartz, D. A., et al. 1979, *ApJ*, 229, L53

- Sikora, M., Begelman, M. C., & Rees, M. J. 1994, *ApJ*, 421, 153
- Sreekumar, P., & Vestrand, W. T. 1997, *IAU Circular* 6776
- Stecker, F. W., & Scully, S. T. 2006, *ApJ*, 652, L9
- Takahashi, T., et al. 1996, *ApJ*, 470, L89
- Takahashi, T., et al. 2000, *ApJ*, 542, L105
- Tanihata, C., et al. 2001, *ApJ*, 563, 569
- Treves A., et al. 1989, *ApJ*, 341, 733
- Ulrich, M.-H., Maraschi, L., & Urry, C. M., 1997, *ARA&A*, 35, 445
- Urry, C. M., et al. 1997, *ApJ*, 486, 799
- Vaughan, S., et al. 2003, *MNRAS*, 345, 1271
- Vestrand, W. T., & Sreekumar, P. 1999, *Astropart. Phys.*, 11, 197
- Vestrand, W. T., Stacy, J. G., & Sreekumar, P. 1995, *ApJ*, 454, L93
- Zhang, Y. H., et al. 1999, *ApJ*, 527, 719
- Zhang, Y. H., et al. 2002, *ApJ*, 572, 762
- Zhang, Y. H., et al. 2005, *ApJ*, 629, 686
- Zhang, Y. H., et al. 2006, *ApJ*, 651, 782
- Zhang, Y. H., & Xie, G. Z. 1996, *A&A*, 116, 289

Table 1. Summary of observations for PKS 2155–304 from 2006 July 28 (MJD 53944) to August 2 (MJD 53944) and the follow-up observations from August 17 (MJD 53964) to 25 (MJD 53972) ^a

Date	N_{tel}	Begin [MJD]	End [MJD]	t_{obs} [hrs]	z [°]	r_{tr} [Hz]
July 28	2	53944.514	53944.663	3.6	29.8	18.7
	3	53944.668	53944.830	3.9	20.4	12.1
July 29	2	53945.522	53945.660	3.1	27.6	14.9
	3	53945.679	53945.762	2.0	12.1	6.2
July 30	2	53946.535	53946.656	2.9	26.1	20.1
	3	53946.668	53946.833	4.0	22.2	12.5
July 31	2	53947.576	53947.653	1.8	19.5	19.8
	3	53947.666	53947.827	3.9	21.7	11.6
Aug. 2	3	53949.658	53949.822	3.9	21.5	11.9
July 28–Aug.2	2			11.4	26.6	18.2
	3			17.6	20.4	11.4
Aug. 17–25	3			19.1	20.9	10.9

^aObservation date, the number of used telescopes, N_{tel} , begin and end time of each observation in MJD, are summarized from the first column to the fourth column. In the following three columns, observation time, t_{obs} , average zenith angle, z , and average trigger rate, r_{tr} are shown. Combined data between July 28 and August 2 are also shown. For the follow-up observations, only combined data are summarized.

Table 2. Summary of results for PKS 2155–304 from 2006 July 28 (MJD 53944) to August 2 (MJD 53944) and the follow-up observations from August 17 (MJD 53964) to 25 (MJD 53972) ^a

Date	N_{tel}	r_{sh} [Hz]	t_{liv} [hrs]	N_{ON}	N_{OFF}	N	$s[\sigma]$	$F(>660\text{GeV})$ ^b
July 28	2	12.4	3.4	675	545	130 ± 29	4.6	3.3 ± 0.7
	3	8.0	3.5	157	132	25 ± 14	1.8	1.0 ± 0.6
July 29 ^c	2	10.2	2.2	338	340	-2.4 ± 20	-0.12	-0.10 ± 0.8
	3	4.1	0.9	39	32	7.1 ± 6.1	1.2	1.3 ± 1.1
July 30	2	13.2	2.8	434	423	11 ± 23	0.48	0.31 ± 1.0
	3	8.1	3.5	235	135	100 ± 16	6.1	3.9 ± 0.6
July 31	2	13.0	1.7	229	224	4.8 ± 17	0.29	2.9 ± 1.0
	3	7.6	3.6	156	135	21 ± 15	1.4	0.81 ± 0.57
Aug. 2	3	7.8	3.5	142	133	9.4 ± 14	0.66	0.38 ± 0.57
July 28–Aug.2	2	12.1	10.1	1676	1532	144 ± 56	2.5	1.3 ± 0.5
	3	7.4	15.0	729	551	178 ± 36	5.0	1.7 ± 0.3
Aug. 17–25	3	7.4	17.1	625	637	-12 ± 36	-0.34	-0.12 ± 0.34 ^d

^aFollowing the observation date and the number of telescopes, average shower rate, r_{sh} , and live time, t_{liv} , are shown in the third and fourth columns, respectively. N_{ON} and N_{OFF} in the fifth and sixth columns are the number of on-source and off-source events, respectively, where the off-source data from July 28 through August 2 were summed up for five nights and normalized to the live time. Seventh column indicates the number of excess events derived by subtraction of off-source events from on-source events, and their significance are shown in the eighth column. Integral flux above 660 GeV are calculated and are shown in the last column. Combined results from July 27 to August 2 and from August 17 and 25 are also presented, respectively.

^bin unit of $\times 10^{-11} \text{ cm}^{-2} \text{ sec}^{-1}$

^caffected by clouds

^dThreshold energy is 680 GeV.

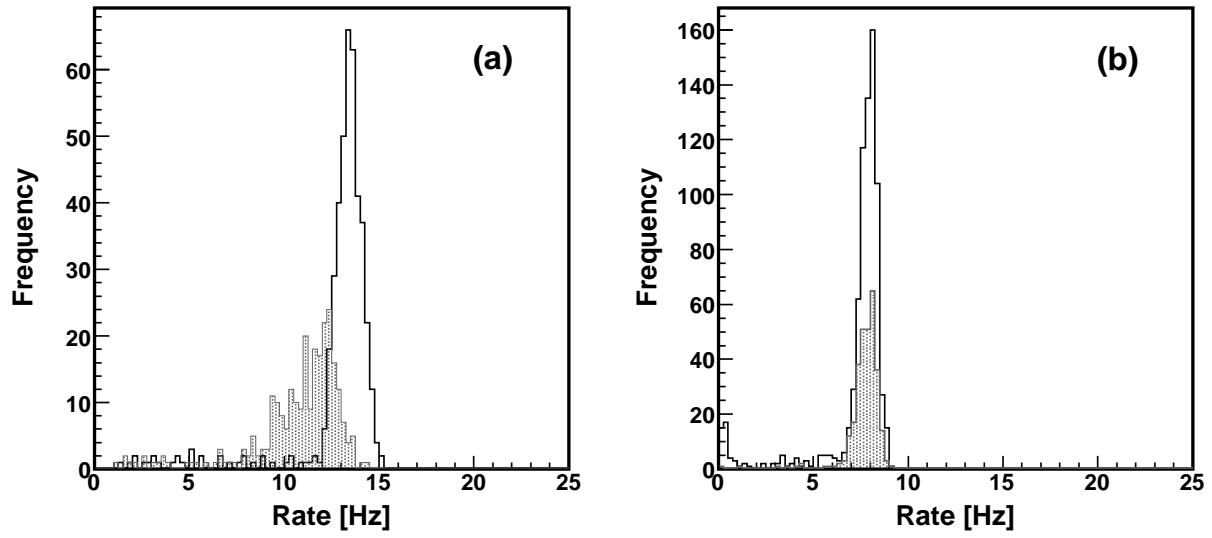


Fig. 1.— Distributions of shower rate after image cleaning for *2fold*(left panel) and *3fold*(right panel). Solid and hatched histograms show ones for zenith angles less than 30° and larger than 30° , respectively. From our analysis we exclude the data whose shower rate are lower than 10 Hz, 8 Hz, and 5 Hz for *2fold-SZ*, *2fold-LZ*, and *3fold*, respectively.

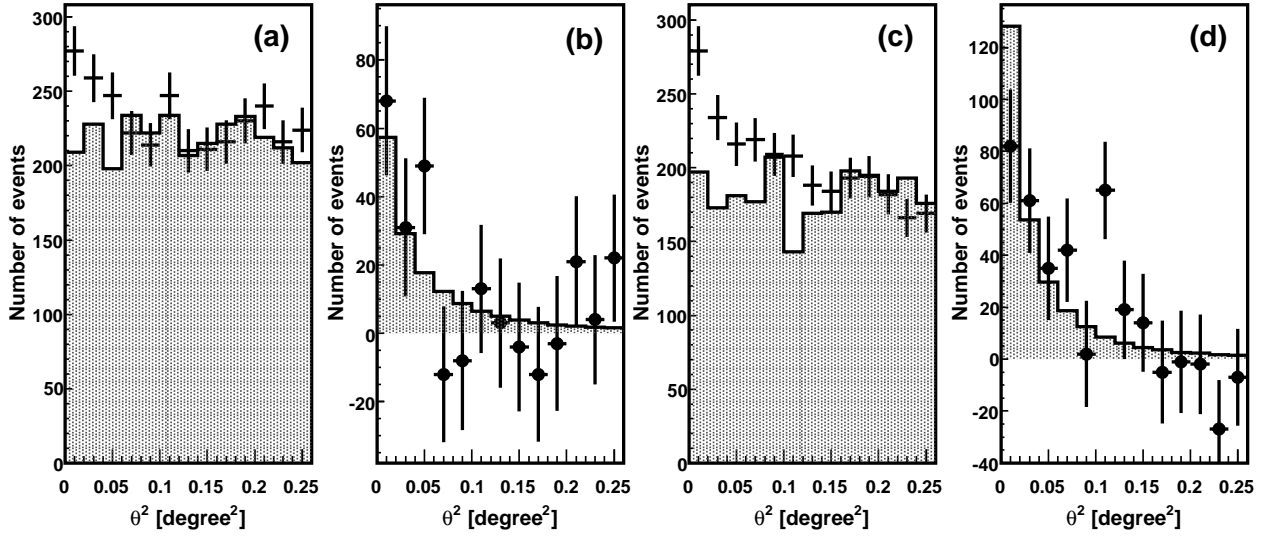


Fig. 2.— Distributions of squared angular distances θ^2 of *2fold* and *3fold* data for PKS 2155–304 in the outburst period, obtained after the FD cut. (a): On-source data (error bars) and off-source data (hatched histogram) for *2fold* are overlaid, where the latter is normalized to the live time (b): Closed circles show the excess events of the on-source above the off-source level for *2fold*. The hatched histogram represents a PSF normalized to the number of excess events in $\theta^2 < 0.25$. (c): Same as (a) for *3fold*. (d): Same as (b) for *3fold*.

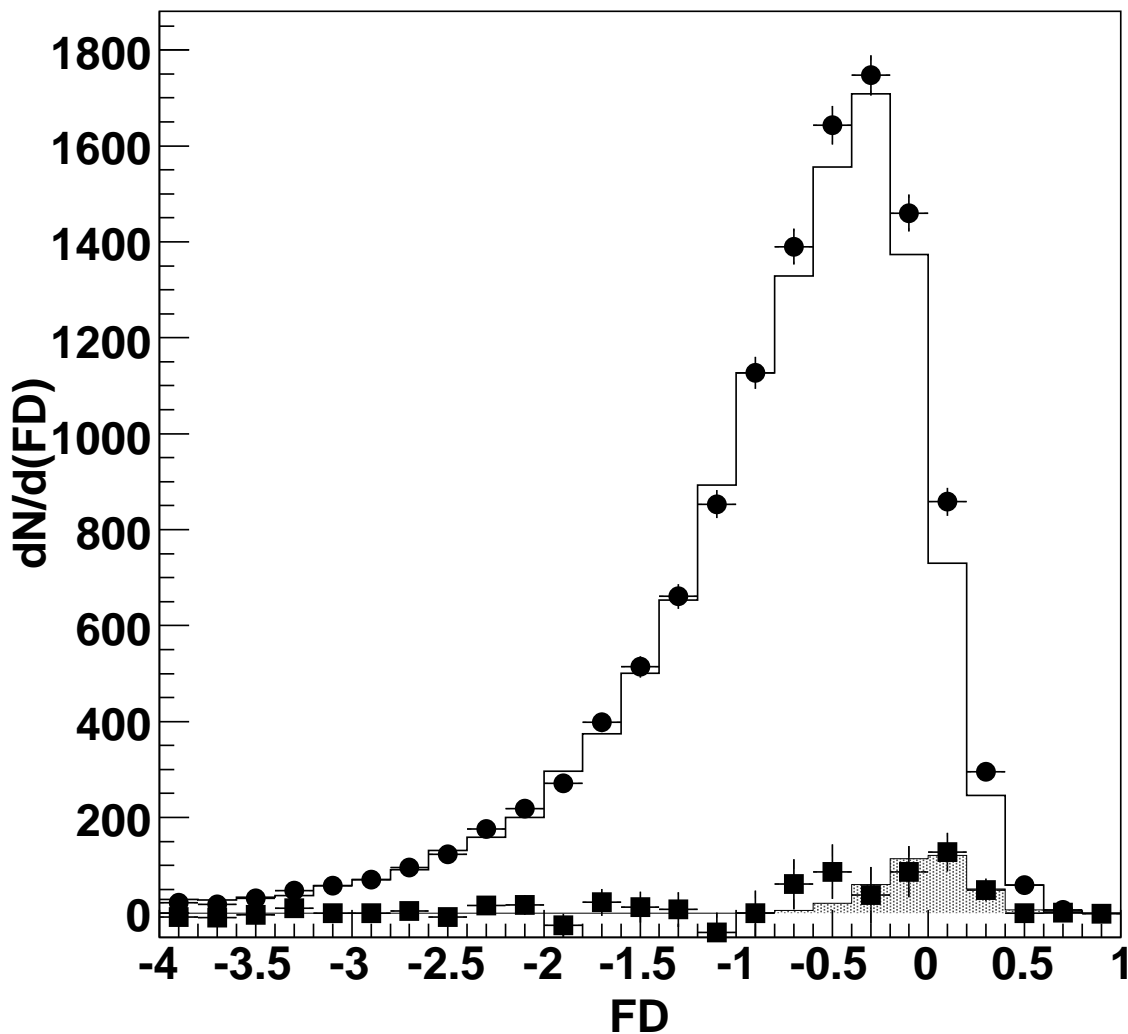


Fig. 3.— Fisher Discriminant (FD) distribution for all events after θ^2 cut in the outburst period. Closed circles with error bars are on-source events ($\theta^2 < 0.06$ for *3fold* data and $\theta^2 < 0.14$ for *2fold*), and a solid histogram indicates off-source events. The closed squares show the distribution of on-off events which are gamma-ray candidates, and a dashed histogram is an expected distribution from Monte Carlo gamma-ray events normalized to the number of excess events.

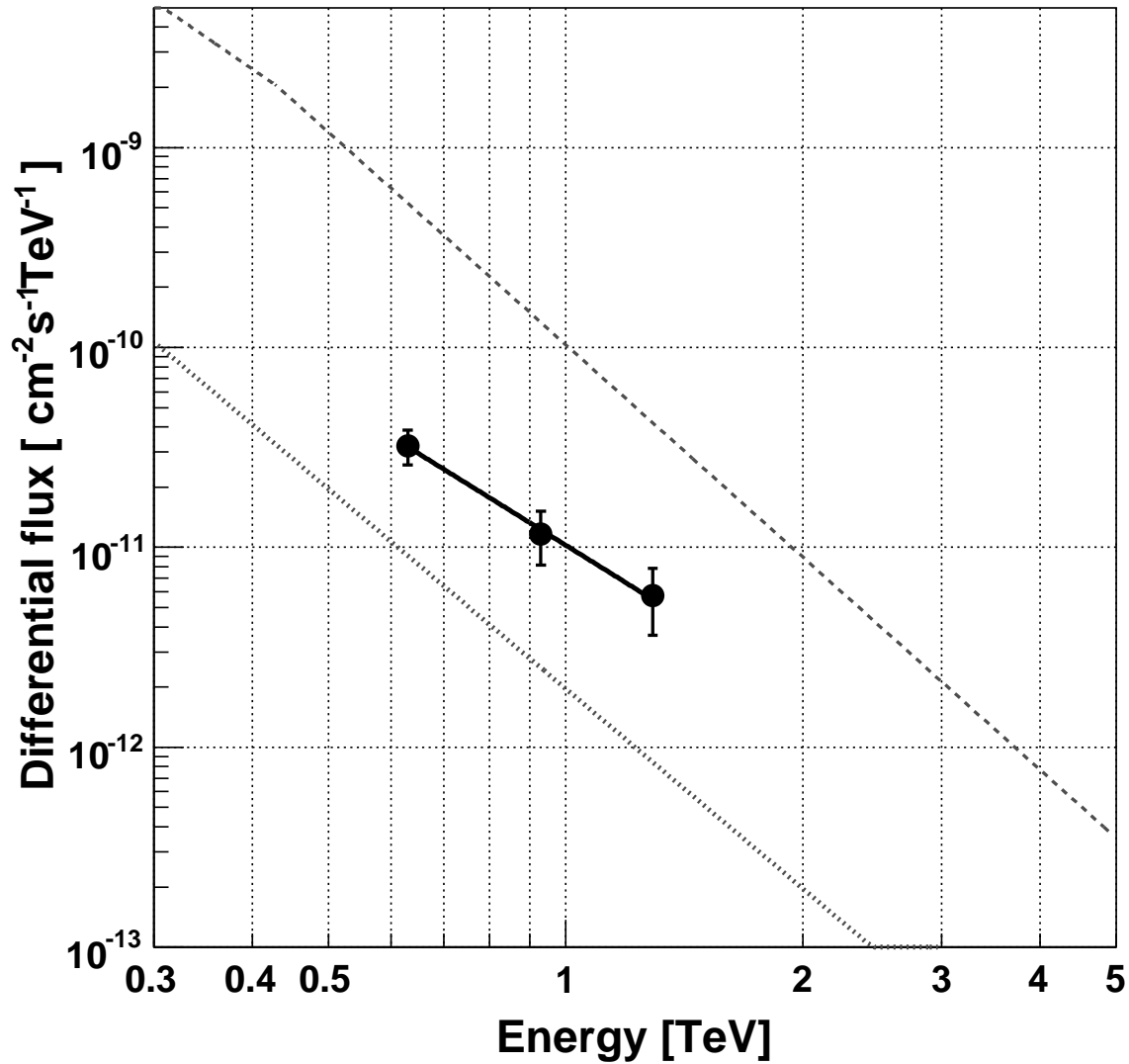


Fig. 4.— Time-averaged differential energy spectrum of PKS 2155–304 between July 28 and August 2. Data plotted by closed circles are obtained from all the data at smaller zenith angle $z < 30^\circ$ (*3fold-SZ* and *2fold-SZ*). The solid line represents the best fit to these data assuming a single power law spectrum. For comparison, the time average differential energy spectra in early July 28 in 2007 reported by Aharonian et al. (2007) during a giant flare and in 2002 and 2003 reported by Aharonian et al. (2005a) at a low state are drawn by dashed and dotted lines, respectively.

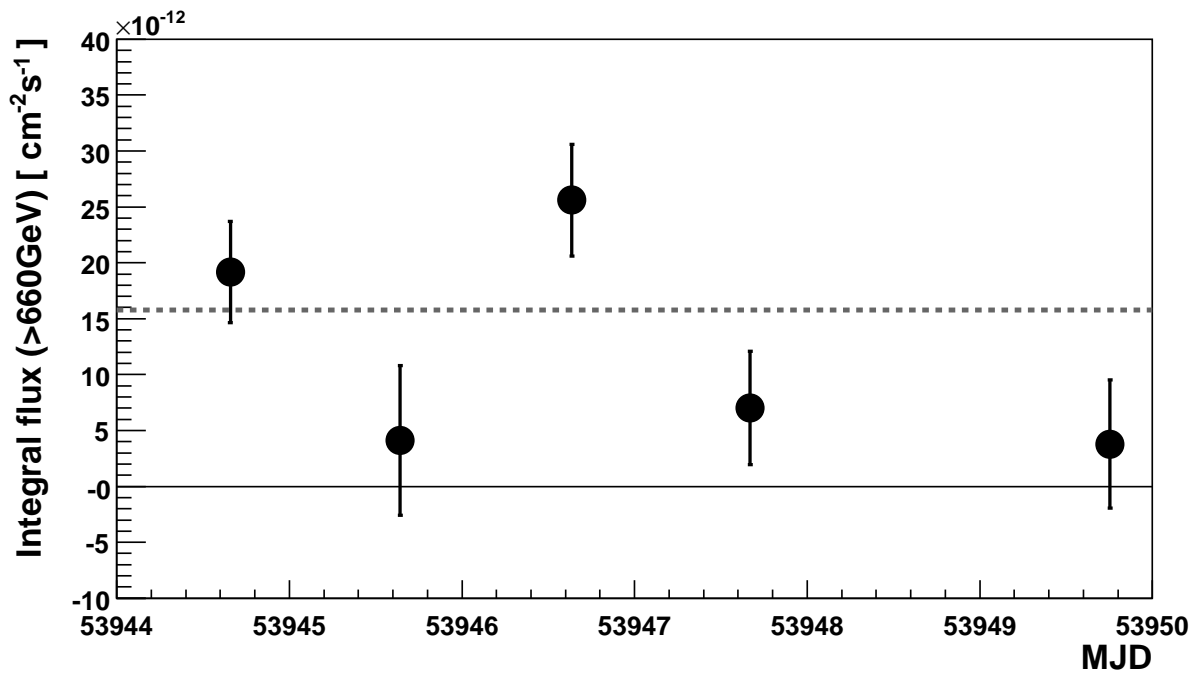


Fig. 5.— Daily average integral flux of PKS 2155–304 using all the data above 660 GeV between 2006 July 28 and August 2. Dashed line indicates an averaged integral flux during this observation period ($\sim 45\%$ Crab flux level).

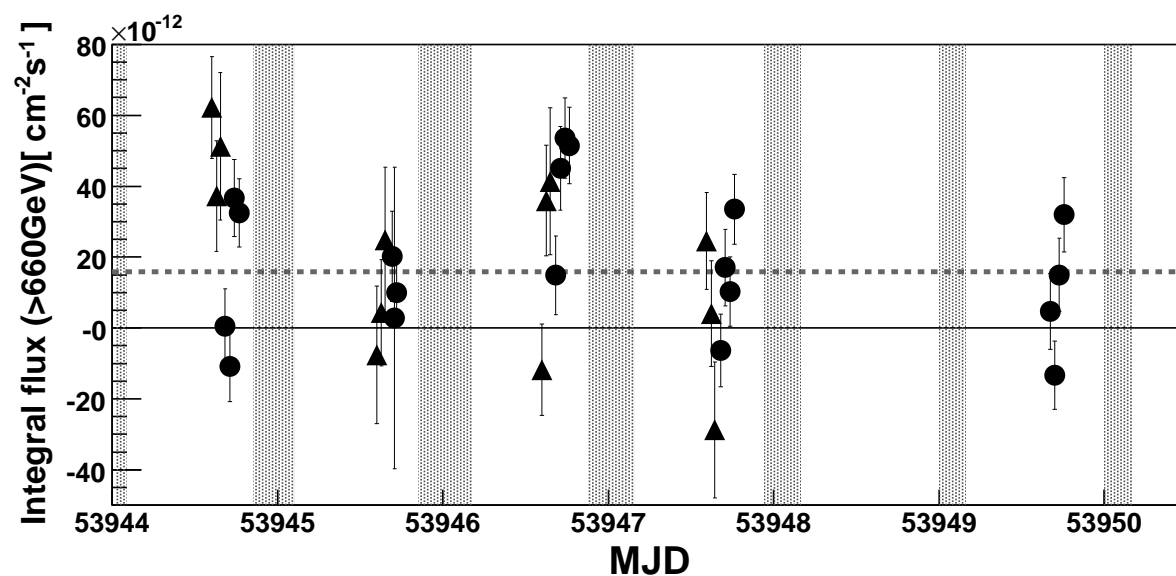


Fig. 6.— Light curve of PKS 2155–304 using all the data at zenith angle less than 30° between 2006 July 28 and August 2, expressed by the integral flux above 660 GeV. Closed triangles and closed circles indicate the results from *2fold-SZ* and *3fold-SZ* datasets, respectively. Dashed line indicates an average integral flux during this observation period. The bin width is 40 minutes. The shaded areas indicate the H.E.S.S. observation periods.

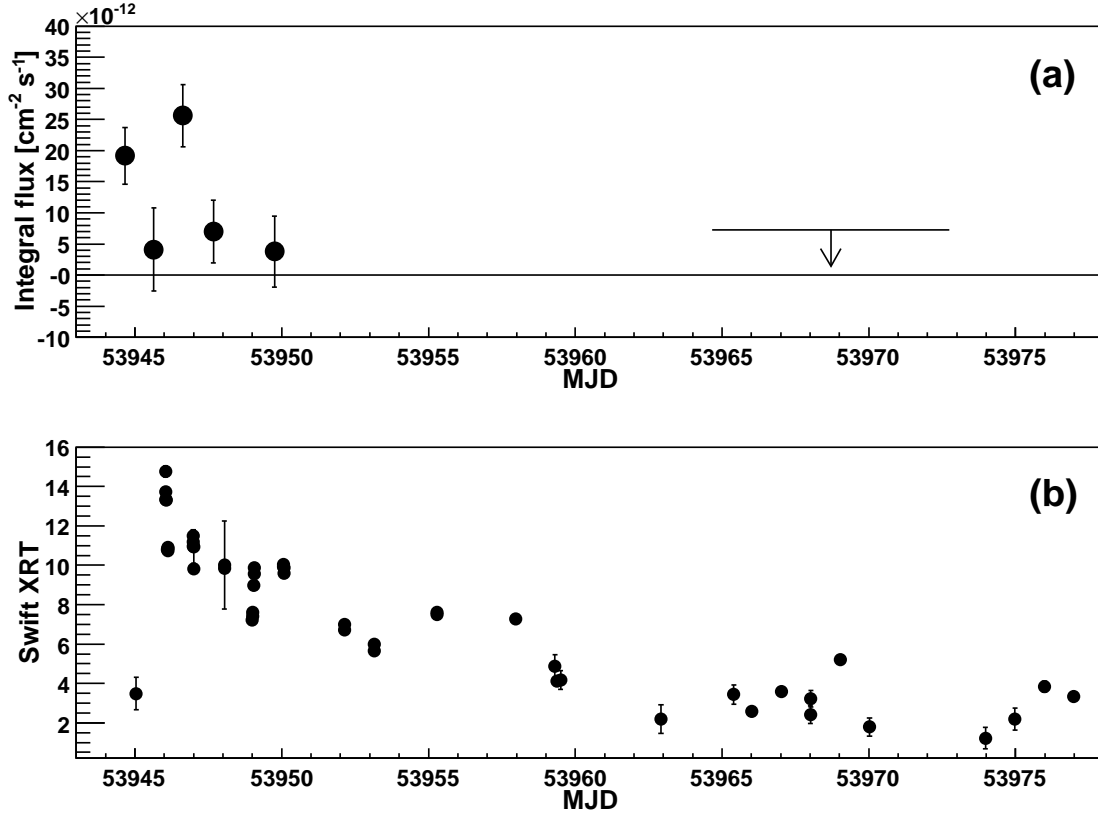


Fig. 7.— Comparison of the light curves between VHE gamma-ray and X-ray bands. (a) A nightly average integral flux of PKS 2155–304 above 660 GeV obtained by the CANGAROO-III given in unit of $\text{cm}^{-2} \text{s}^{-1}$, which is the same as in Fig. 5. An upper limit of the integral flux between August 17 and 25 is also plotted, which is an extrapolate value from the actual upper limit above 680 GeV. (b) X-ray [0.3–10 keV] counts in unit of count s^{-1} from the XRT on *Swift* (Foschini et al. 2007).